



Topological amplification and frequency conversion in a photonic lattice with a two-photon driving

Ling-Xia Guo , Liang-Liang Wan ,* Liu-Gang Si, and Ying Wu*School of Physics, Huazhong University of Science and Technology, Wuhan 430074, China*

(Received 17 March 2023; revised 7 June 2023; accepted 7 July 2023; published 20 July 2023)

We investigate the topological amplification and frequency conversion of a one-dimensional photonic lattice subjected to a two-photon driving, considering both the thermodynamic- and dynamical-stability regimes. Our analysis shows that the critical behavior of their stability occurring at zero energy depends on the width of the lower band, as well as the strength and phase of the two-photon driving. We demonstrate that the presence of the driving field does not alter the band topology of the system under both regimes, and we showcase the nontrivial band topology. The occurrence of edge modes within the band gap is also demonstrated by employing a Bogoliubov (squeezed-state) representation. Furthermore, we show the amplification and frequency conversion of edge modes using the input-output formalism, relying on the mechanism of an optical parametric amplifier. These phenomena exhibit an absence-to-presence transition at a critical value of hopping strength, signifying a topological phase transition. Additionally, we demonstrate the robustness of these phenomena against symmetry-preserving disorders. Our findings have potential applications in engineering fault-tolerant quantum-optics devices based on the topological protection.

DOI: [10.1103/PhysRevA.108.013512](https://doi.org/10.1103/PhysRevA.108.013512)

I. INTRODUCTION

The insights gained from the topological states of quantum matter in condensed-matter physics have been widely applied to optical systems, leading to the realization of photonic analogs of the quantum Hall effect [1–5]. These developments have opened up broad prospects for achieving unidirectional (chiral) optical transmission [6–8]. However, the lack of magneto-optical response in the optical domain poses a significant obstruction to implementing other topological models in photonic materials. To address this challenge, the pseudo-time-reversal symmetry has been introduced by incorporating an additional degree of freedom, enabling the realization of analogs of the quantum spin Hall effect for photons [7,9–14]. Alternatively, periodically driving the system in time has also been shown to give rise to unconventional topological properties, as demonstrated in the photonic Floquet Chern insulator [15,16]. The intense activity in various photonic systems with nontrivial topological structures has prompted the development of the emerging field of topological photonics [17–20].

While previous works have primarily focused on the quantum simulation of topological insulators, there have been remarkable advancements featuring the bosonic nature [21–43]. For instance, in the context of cold-atom systems, the realization of the interaction-driven topological superfluid has been evidently reported [41]. The associated band topology is governed by a Bogoliubov Hamiltonian within the mean-field approximation, and it exhibits an exotic pseudounitary structure that sets it apart from super-

conductors [21,44–46]. Meanwhile, a dedicated topological classification framework has been developed for quadratic bosonic systems [47–51], which is distinct from the well-known Altland-Zirnbauer classification [52]. Additionally, the bosonic pairing field (particle-number-nonconserving term), which intrinsically describes a parametric amplification process [53], can be treated as a spin-orbit coupling capable of opening topological gaps in two- and three-dimensional systems [54]. Intriguingly, irrespective of the stability concerns, the bosonic pairing field can even lead to the amplification of edge states [26,36,55]. These works highlight the pivotal role of the particle-number-nonconserving term in exploring exotic topological phenomena in photonic systems.

In this paper, we study a one-dimensional (1D) photonic system with $\chi^{(2)}$ nonlinear interaction. By coherently pumping the auxiliary mode, such a system can be reduced to a dimer chain with a two-photon driving term. Attributed to the parametric amplification process, the critical behavior occurs in the transition from thermodynamic and dynamical stability to instability and depends on the strength and relative phase of the two-photon driving, as well as the width of the lower band. Apart from this, we demonstrate that the presence of two-photon driving does not alter the band topology characterized by the winding number in both stability regimes. Applying the open boundary condition, the edge modes can be obtained analytically when the winding number is nonvanishing.

Interestingly, our finding reveals the intriguing amplification and frequency conversion of an incoming field, which correspond to the elastic- and inelastic-scattering processes, respectively, within the input-output formalism. These phenomena relying on the mechanism of an optical parametric amplifier undergo an absence-to-presence transition at a critical value of hopping strength, which corresponds to a

*wanlianghust@163.com

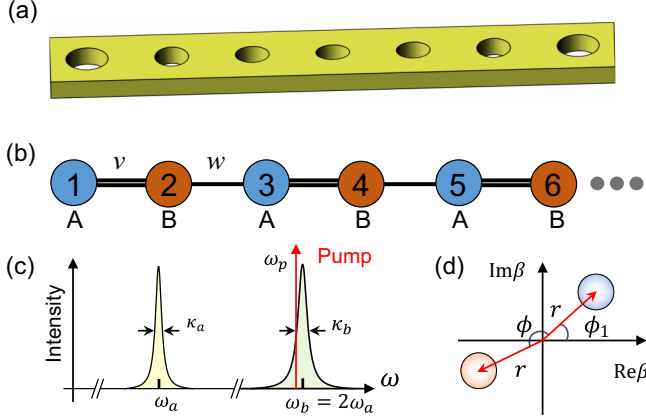


FIG. 1. (a) Schematic of a 1D photonic crystal. The modified pattern of holes generates a point defect hosting a local optical mode. (b) The dimer chain, i.e., Su-Schrieffer-Heeger model, with hopping rates $v = t - \delta$ and $w = t + \delta$ for the intra- and intercell sites, respectively. (c) Spectrogram of a local $\chi^{(2)}$ nonlinear interaction at site j . The Lorentzian spectral lines denote the optical mode \hat{a}_j (\hat{b}_j) with frequency ω_a (ω_b) and decay rate κ_a (κ_b) at site j . This interaction describes a degenerate three-wave mixing process and involves two optical modes \hat{a}_j (yellow) and \hat{b}_j (green) with the frequency $\omega_a = \omega_b/2$. The auxiliary mode is coherently pumped by a driving field (red arrow) with frequency ω_p . (d) The quadratures of the coherent state of the auxiliary modes in a unit cell, $\langle \hat{b}_j \rangle = \beta_j e^{-i\omega_p t}$. Here $\beta_j = r e^{i\phi_1}$ (blue) for odd j and $\beta_j = r e^{i\phi_2}$ (red) for even j , where $r \in \mathbb{R}$, $\phi_1, \phi_2 \in [-\pi, \pi)$ and $\phi = \phi_2 - \phi_1$.

topological phase transition. We also demonstrate the robustness of these phenomena against symmetry-preserving disorders. In addition, the proposed model can be implemented in various platforms, including coupled cavity arrays [56–59], superconducting circuits [60–63], and photonic crystals based on the optomechanical interaction [64,65]. Our paper opens up possibilities for engineering fault-tolerant quantum-optics devices utilizing topological protection, such as topological transducers, modulators, switches, etc.

Our paper is organized as follows. We first introduce our system and derive its effective Hamiltonian in Sec. II, and discuss both the thermodynamic and dynamical stability in Sec. III. Section IV is devoted to the topological structure of the system and the emergence of edge modes arising from the bulk-edge correspondence under the two-photon driving. In Sec. V, the topological amplification and frequency conversion are demonstrated by examining the elastic- and inelastic-scattering processes of the system to an incoming field, respectively. Then, we show the robustness of these topological phenomena against symmetry-preserving disorders in Sec. VI. We discuss experimental implementations in Sec. VII and provide a discussion on the relevant literature in Sec. VIII. Finally, our conclusion is made in Sec. IX.

II. SYSTEM AND HAMILTONIAN

Let us consider a 1D photonic crystal, i.e., dielectric material with an appropriate pattern of holes that creates the complete optical band gaps [66]. As schematically shown in Fig. 1(a), a local modification of the hole pattern at some place

in the crystal generates a point defect that hosts the localized optical mode. A 1D photonic lattice can be produced by designing a periodic array of such point defects. Each localized mode exhibits an evanescent overlap with the adjacent sites, resulting in the hopping of photons. Based on this design, we can then obtain a 1D dimer chain, also known as the Su-Schrieffer-Heeger (SSH) model, as shown in Fig. 1(b). The Hamiltonian of this chain can be written as ($\hbar = 1$)

$$\hat{H} = \sum_{j=1}^{2N} [\omega_a \hat{a}_j^\dagger \hat{a}_j + (t + \delta e^{i\pi j}) (\hat{a}_{j+1}^\dagger \hat{a}_j + \text{H.c.})], \quad (1)$$

where \hat{a}_j (\hat{a}_j^\dagger) denotes the annihilation (creation) operator of the localized optical mode with frequency ω_a at site j . Here $v = t - \delta$ and $w = t + \delta$ with $0 \leq |\delta| \leq t$ are the hoppings of photons between the intra- and intercell sites, respectively, and N is the number of unit cells of the dimer chain.

Suppose that the photonic material has the $\chi^{(2)}$ nonlinear effect. The nonlinearity interaction is depicted by a local three-wave mixing process and governed by the Hamiltonian $\hat{H}_{\text{int}} = \sum_{j=1}^{2N} (G \hat{a}_j^\dagger \hat{a}_j^\dagger \hat{b}_j + \text{H.c.})$, where \hat{b}_j (\hat{b}_j^\dagger) denotes the annihilation (creation) operator of the auxiliary mode with frequency ω_b at site j . It satisfies the frequency-matching condition $\omega_b = 2\omega_a$ [see Fig. 1(c)]. Here $G \in \mathbb{R}$ represents the interaction strength. By coherently pumping the auxiliary mode at site j , its bosonic operator can be classically treated, $\hat{b}_j \rightarrow \langle \hat{b}_j \rangle = \beta_j e^{-i\omega_p t}$ [see Fig. 1(d)], where $\beta_j = r e^{i\phi_j}$ (i.e., $r = |\beta_j|$ and $\phi_j = \arg \beta_j$) and ω_p ($< \omega_b$) is the frequency of the pump field. Then, this interaction can be effectively reduced to a two-photon driving field, which is given by the time-dependent particle-number-nonconserving Hamiltonian $\hat{H}_{\text{sqz}} = \frac{1}{2} \sum_j \lambda_j \hat{a}_j^\dagger \hat{a}_j^\dagger e^{-i\omega_p t} + \text{H.c.}$ with $\lambda_j = 2G\beta_j$. This two-photon driving \hat{H}_{sqz} describes an optical parametric amplification process [53]. It respects the translation-invariant symmetry, and its phase at each site is given by $\phi_{2n-1} = \arg \lambda_{2n-1} \equiv \phi_1$ and $\phi_{2n} = \arg \lambda_{2n} \equiv \phi_2$ with $n = 1, 2, \dots, N$. Performing a global $U(1)$ gauge transformation, $\hat{a}_j \rightarrow \hat{a}_j e^{i\phi_j/2}$ ($j = 1, 2, \dots, 2N$), we obtain $\hat{H}_{\text{sqz}} = \frac{1}{2} \sum_{n=1}^N \lambda (\hat{a}_{2n-1}^\dagger \hat{a}_{2n-1}^\dagger + e^{i\phi} \hat{a}_{2n}^\dagger \hat{a}_{2n}^\dagger) e^{-i\omega_p t} + \text{H.c.}$, where $\lambda = |\lambda_j|$ and $\phi = \phi_2 - \phi_1$ is the relative phase between sites in a unit cell. Note ϕ cannot be fully reduced since the $U(1)$ symmetry breaks down.

In the rotating framework at frequency $\omega_p/2$, the total Hamiltonian becomes time independent:

$$\begin{aligned} \hat{H}_{\text{eff}} = & \sum_{j=1}^{2N} [\omega_0 \hat{a}_j^\dagger \hat{a}_j + (t + \delta e^{i\pi j}) (\hat{a}_{j+1}^\dagger \hat{a}_j + \text{H.c.})] \\ & + \frac{\lambda}{2} \sum_{n=1}^N (\hat{a}_{2n-1}^\dagger \hat{a}_{2n-1}^\dagger + e^{i\phi} \hat{a}_{2n}^\dagger \hat{a}_{2n}^\dagger + \text{H.c.}), \quad (2) \end{aligned}$$

where $\omega_0 = \omega_a - \omega_p/2 > 0$. It describes the SSH model with a two-photon driving term. Under the assumption of the translation invariance and periodic boundary condition, \hat{H}_{eff} can be transformed into crystal-momentum space by the Fourier transformation with $\hat{a}_k = \frac{1}{\sqrt{N}} \sum_{j=1}^{2N} e^{-ikj/2} \hat{a}_j$ and $\hat{a}_k^\dagger = \frac{1}{\sqrt{N}} \sum_{j=1}^{2N} e^{ikj/2} \hat{a}_j^\dagger$. Here the lattice spacing is set to be 1 for simplicity. Using the Nambu spinor

$\hat{\Phi}_k = (\hat{a}_{kA}, \hat{a}_{kB}, \hat{a}_{-kA}^\dagger, \hat{a}_{-kB}^\dagger)^T$ with subscripts A and B depicting the sublattice indices, the Hamiltonian (2) can be rewritten as $\hat{H}_{\text{eff}} = \frac{1}{2} \sum_k \hat{\Phi}_k^\dagger H_{\text{eff}}(k) \hat{\Phi}_k$, where

$$H_{\text{eff}}(k) = \begin{pmatrix} H_0(k) & H_s \\ H_s^* & H_0^T(-k) \end{pmatrix} \quad (3)$$

is the Bogoliubov Hamiltonian. Here $H_0(k) = \omega_0 I + d_x(k)\sigma_x + d_y(k)\sigma_y$ with $d_x(k) = v + w \cos k$ and $d_y(k) = w \sin k$, and $H_s = \lambda \text{diag}(1, e^{i\phi})$. σ_i ($i = x, y, z$) denotes the conventional Pauli matrices. By performing the pseudounitary diagonalization [67,68], we then obtain the spectrum of the system:

$$E_{\pm}^2(k) = \omega_0^2 + d^2 - \lambda^2 \pm 2d\sqrt{\omega_0^2 - \lambda^2 \sin^2 \frac{\phi}{2}}, \quad (4)$$

where $d = \sqrt{d_x^2 + d_y^2} = \sqrt{v^2 + w^2 + 2vw \cos k}$. Here, the k dependence of d_x and d_y is suppressed temporarily for brevity. In the absence of two-photon driving ($\lambda = 0$) corresponding to the bare (linear) SSH model, the Bloch spectrum located at ω_0 has a band gap $4|\delta|$ and the bandwidth is given by $2 \min\{v, w\}$. Its Bloch spectrum will be changed in the presence of the time-independent two-photon driving field (H_s). If $[\omega_0 - d(k)]$ is close to zero energy, the critical behavior of stability can even occur.

III. ANALYSIS ON STABILITY

The particle-number-nonconserving term intrinsically induces non-Hermiticity in bosonic Bogoliubov Hamiltonians, and can lead to instability. For a general quadratic-bosonic system, two types of stability are typically of concern: thermodynamic stability [50,51] and dynamical stability [69]. Thermodynamic stability, also known as Landau stability [70], requires the system energy to be non-negative ($E \geq 0$). Dynamical stability refers to the condition where the spectrum is real ($E \in \mathbb{R}$) and the Bogoliubov Hamiltonian can be pseudounitarily diagonalized. At first glance, the thermodynamic-stability regime is naturally encompassed within the dynamical-stability regime. However, they have a crucial difference, as the thermodynamic-stability regime may involve the occurrence of a Jordan block at zero energy during the diagonalization [44,45]. The Jordan block corresponds to an exceptional point, where the system fails to satisfy the dynamical-stability regime [71]. This optical system of interest can reside in either of these stability regimes.

In the thermodynamic-stability regime, the Bloch spectrum (4), more explicitly, the minimum value of the lower band, is either greater than or equal to zero energy, i.e., $E_-(k=0) \geq 0$. This condition provides a criterion for diagnosing the critical behavior of the transition from thermodynamic stability to instability, which is given by

$$\omega_0^2 + 4t^2 - \lambda^2 = 4t\sqrt{\omega_0^2 - \lambda^2 \sin^2 \frac{\phi}{2}}. \quad (5)$$

The equality indicates that the minimum value of the lower band is zero, $E_-(0) = 0$ [see Fig. 2(a)]. On the other hand, the system can be dynamically stable even though its spectrum contains energies below zero. In order to avoid unnecessary repetition, the consideration of the dynamical-stability

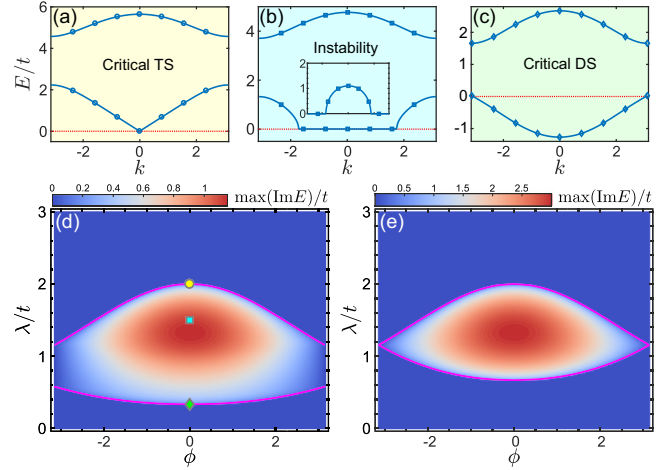


FIG. 2. [(a)–(c)] Bloch spectra of the system with $\lambda = 2t$ in (a), $\lambda = 3t/2$ in (b), and $\lambda = t/3$ in (c). They correspond to the circle (yellow), square (cyan), and diamond (green) marks in (d), respectively. TS (DS) indicates the thermodynamic stability (dynamical stability). The panel in (b) illustrates the imaginary part of the spectrum. Here $\delta = \pm t/2$ and $\omega_0 = 2\lambda$. [(d),(e)] Stability diagrams for $\delta = \pm t/2$ (d) and $\delta = \pm t$ (e). The relevant parameter is $\omega_0 = 2\lambda$. The color represents the maximum value of the imaginary part of the spectrum and the magenta color labels the critical curves.

regime in this context excludes cases that overlap within the thermodynamic-stability regime. Given this consideration, in the dynamical-stability regime, the maximum value of the lower band satisfies $E_-(k = \pi) < 0$. The system exhibits a critical behavior of transition from dynamical stability to instability when $E_-(\pi) = 0$, as illustrated in Fig. 2(c). Using this condition, one can derive the same formula as Eq. (5) by the replacement $t \rightarrow |\delta|$. Apart from these two stability regimes, the system is dynamically unstable, where the imaginary part of the spectrum is nonzero, as depicted in Fig. 2(b).

Next, we will show the critical behavior for the thermodynamic- and dynamical-stability regimes. Figures 2(d) and 2(e) plot the imaginary part of the spectrum of the system under the parameter conditions of $|\delta| = t/2$ and $|\delta| = t$, respectively. The nonzero imaginary one indicates the occurrence of instability. In these plots, the parameter regions enclosed by the magenta curves resemble an “eye” shape, corresponding to the unstable region of the system. These curves are derived by the criterion in two regimes. Explicitly, the upper and lower curves correspond to the criticality for the thermodynamic- and dynamical-stability regimes, respectively. Additionally, both figures show the dependence of stability on the strength λ and relative phase ϕ between the sublattices A and B . Through some calculations, one can easily derive the formula from Eq. (5) for the thermodynamic-stability regime, which is given by $\lambda = \frac{2}{3}t(\sqrt{4 - \sin^2 \frac{\phi}{2}} + \cos \frac{\phi}{2})$. Similarly, by the replacements $t \rightarrow |\delta|$ and $+ \rightarrow -$, we obtain a similar formula for the dynamical-stability regime. It turns out that as $|\delta|$ increases to t (i.e., the bandwidth of the bare SSH model, $2 \min\{v, w\}$, decreases), the region of the eye shape becomes smaller. In particular, when $|\delta| = t$ [see Fig. 2(e)], the system of interest is explicitly reduced

to a highly degenerate two-mode system. It suggests that the stability of the system critically depends on the strength and phase of the two-photon driving, as well as the width of the lower bands.

It should be noted that the critical behavior can be adjusted or even eliminated by the relative phase ϕ . To achieve this, we perform a Bogoliubov (squeezing) transformation

$$\begin{aligned}\hat{\alpha}_{kA} &= \cosh \chi \hat{a}_{kA} + \sinh \chi \hat{a}_{-kA}^\dagger, \\ \hat{\alpha}_{kB} &= \cosh \chi \hat{a}_{kB} + e^{i\phi} \sinh \chi \hat{a}_{-kB}^\dagger,\end{aligned}\quad (6)$$

where the squeezing factor χ is determined by $\tanh 2\chi = \lambda/\omega_0$. In this new quasiparticle basis (squeezed-state representation), the two-photon driving term disappears. Instead, a new particle-number-nonconserving term arises, given by

$$\cosh \chi' \sum_k [e^{-i\phi'} (v + w e^{ik}) \hat{\alpha}_{kA} \hat{\alpha}_{-kB} + \text{H.c.}],$$

where $\chi' = 2\chi |\cos \frac{\phi}{2}|$ and $\phi' = \arg(1 + e^{i\phi})$ for $\phi \in (-\pi, \pi)$. This term corresponds to a nondegenerate parametric amplification process, and its existence individually induces instability. When $\phi = 0$, $\cosh \chi'$ reaches its maximum value. Varying ϕ from zero to π while other parameters are fixed, $\cosh \chi'$ decreases and, thus, the influence of this term diminishes. This term disappears when the phase-anti-matching condition is satisfied, $\phi = \pi$. In this case, the Bloch bands are given by $E_{\pm}(k) = \tilde{\omega}_0 \pm d(k)$ with $\tilde{\omega}_0 = \sqrt{\omega_0^2 - \lambda^2}$. Accordingly, the critical behavior also disappears even if the lower band $E_-(k)$ crosses zero energy, provided that $\omega_0 > \lambda$. The condition for dynamical stability [i.e., $E_-(k) < 0$] is thus relaxed.

IV. NONTRIVIAL BAND TOPOLOGY AND EDGE MODE

Now, let us analyze the symmetry and band topology of the system. In the absence of the two-photon driving, the system possesses sublattice symmetry, given by

$$SH(k)S^{-1} = -H(k), \quad (7)$$

where $H(k) = d_x(k)\sigma_x + d_y(k)\sigma_y$ represents the single-particle Hamiltonian in the interaction picture with respect to the frequency ω_a , and $S = \sigma_z$ is the symmetry operator. According to the Altland-Zirnbauer classification [52], a 1D lattice system with such symmetry belongs to class AIII (see Appendix A for further details). The associated band topology is characterized by a winding number, which is defined as

$$W = \int_0^{2\pi} \frac{dk}{4\pi i} \text{Tr} \left[S(H(k))^{-1} \frac{\partial}{\partial k} H(k) \right]. \quad (8)$$

When the band gap is open ($\delta \neq 0$), the band topology is well defined. In particular, the winding number (8) is either nonvanishing for $\delta > 0$ or vanishing for $\delta < 0$, corresponding to the nontrivial and trivial band topology, respectively. Apart from the mathematical description, the band topology can also be visualized using a two-dimensional auxiliary space, denoted as d_x - O - d_y , as illustrated in Fig. 3(a). The origin point represents the topological obstruction of such system. One can see that the components $d_x(k)$ and $d_y(k)$ of the Hamiltonian form a circle in the auxiliary space. The circle intersects this point, corresponding to the case where the band gap is closed

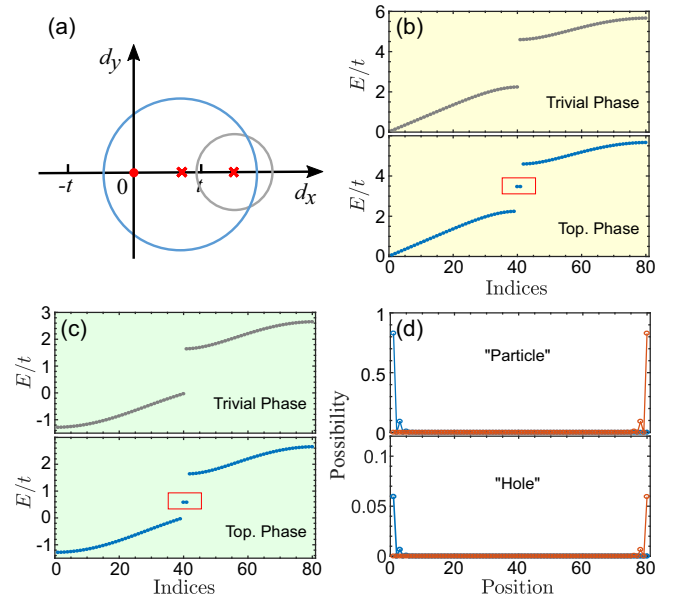


FIG. 3. (a) Two-dimensional auxiliary space constructed by $d_x(k)$ and $d_y(k)$. The blue circle corresponding to $\delta > 0$ encloses the origin point, while the gray circle corresponding to $\delta < 0$ does not. (b), (c) Spectra of the system under the open boundary condition. The upper (lower) panels depict the trivial (nontrivial) band topology with $\delta = -t/2$ ($\delta = t/2$). For the nontrivial (trivial) band topology, edge modes (highlighted inside the red boxes) appear (disappear). The cases in (b) and (c) correspond to Figs. 2(a) and 2(c), respectively. (d) Possibility distribution of the edge modes in (b) and (c) in terms of “particle” and “hole.”

(i.e., $\delta = 0$) and the topology is ill defined. When the point lies inside (outside) the circle, the topology is nontrivial (trivial), which corresponds to the condition $\delta > 0$ ($\delta < 0$).

Next, we incorporate the two-photon driving term into our analysis to investigate its influence on the band topology of the system. Based on the fact that the topology remains unchanged under any continuous deformations without closing the band gap [72], we focus on the band gap of the Bloch spectrum (4), defined as

$$\Delta = \min E_+(k) - \max E_-(k). \quad (9)$$

The minimum value of the upper band and the maximum value of the lower band occur simultaneously at $k = \pi$. From Eq. (9), the band gap is closed if $E_+(\pi) = E_-(\pi)$.

In the thermodynamic-stability regime, where $E_-(0) \geq 0$, the condition for closing the band gap, $\Delta = 0$, can be simplified to

$$\delta \sqrt{\omega_0^2 - \lambda^2 \sin^2 \frac{\phi}{2}} = 0. \quad (10)$$

Due to $\omega_0 > \lambda$ in this regime, the condition (10) becomes $\delta = 0$. This implies that the existence of the band gap depends on the value of δ and is independent of the two-photon driving term. Therefore, in the thermodynamic-stability regime, the two-photon driving term cannot alter the band topology of the system.

In the dynamical-stability regime for $\phi \in (-\pi, \pi)$, the band gap is closed if $\lambda = \sqrt{\omega_0^2 + 4\delta^2}$ and $\tan \frac{\phi}{2} = \pm \omega_0/2\delta$.

However, the eigenenergies and the associated eigenstates both coalesce at this point, corresponding to an exceptional point [71]. Thus, this situation does not fall within the scope of the dynamical-stability regime. For the special case $\phi = \pi$, the bands $E_{\pm}(k) = \tilde{\omega}_0 \pm d(k)$ yield a gap $\Delta = 4|\delta|$. It is obvious that the gap is independent of the two-photon driving term, too. In a short summary, unlike the behavior observed in systems with cross-Kerr interaction [28,73], the driving term does not alter the band topology in both regimes. In other words, in the presence and/or absence of the two-photon driving term, whether the system exhibits the nontrivial band topology is determined by the value of δ .

According to the bulk-edge correspondence, the presence of nontrivial band topology implies the existence of edge modes within the band gap when the open boundary condition is applied. Figures 3(b) and 3(c) plot the spectrum in the open boundary condition, corresponding to Figs. 2(a) and 2(c), respectively. The edge mode occurs for $\delta = t/2$ and disappears for $\delta = -t/2$. Such a numerical result is consistent with the prediction based on the winding number (8). It is worth noting that the parameter condition in Fig. 3(c) can be treated as the limit of the dynamical-stability regime. In order to analyze the edge mode, we focus on the phase-anti-matching condition $\phi = \pi$ based on the topological property. In the quasiparticle basis of Eq. (6), the edge modes can be constructed as

$$\hat{\alpha}_L = \sum_{n=1}^N \xi^{n-1} \hat{\alpha}_{2n-1}, \quad \hat{\alpha}_R = \sum_{n=1}^N \xi^{N-n} \hat{\alpha}_{2n}, \quad (11)$$

where L and R represent the left and right ends of the 1D lattice, respectively, and $\xi = -v/w$ ($|\xi| < 1$). These modes satisfy the commutation relations

$$\begin{aligned} [\hat{\alpha}_L, \hat{H}_{\text{eff}}] &= \tilde{\omega}_0 \hat{\alpha}_L + O(\xi^N), \\ [\hat{\alpha}_R, \hat{H}_{\text{eff}}] &= \tilde{\omega}_0 \hat{\alpha}_R + O(\xi^N). \end{aligned} \quad (12)$$

It shows that the two edge modes (11) with energy $\tilde{\omega}_0$ are conserved quantities, as the last term in Eq. (12) vanishes in the thermodynamic limit ($N \rightarrow \infty$). This confirms that the edge modes $\hat{\alpha}_{L,R}$ are indeed the modes of the system. Figure 3(d) depicts the edge modes (11) composed of the annihilation and creation operators, which can be interpreted as the ‘‘particle’’ and ‘‘hole’’ components, respectively [24,74]. We note that these two components exhibit the same distribution profile. To explain this, we transform the edge modes into the original basis as follows:

$$\begin{aligned} \hat{\alpha}_L &= \sum_{n=1}^N \xi^{n-1} (\cosh \chi \hat{a}_{2n-1} + \sinh \chi \hat{a}_{2n-1}^{\dagger}), \\ \hat{\alpha}_R &= \sum_{n=1}^N \xi^{N-n} (\cosh \chi \hat{a}_{2n} - \sinh \chi \hat{a}_{2n}^{\dagger}). \end{aligned} \quad (13)$$

Equation (13) shows that the hole components of the edge modes are proportional to the particle ones with a ratio of $\tanh \chi$, which originates from the two-photon driving.

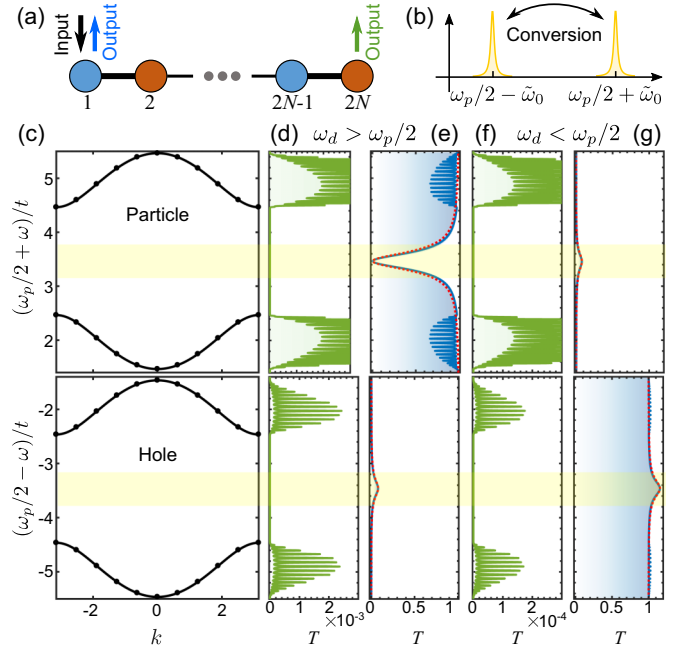


FIG. 4. (a) Schematic of the setup for detection. There are two waveguides coupled to the left end site of the 1D photonic lattice for injecting the probe field (black arrow) and detecting the response (blue arrow) of the system, respectively. One waveguide is coupled to the right end site for detecting the response (green arrow) at this end. (b) Frequency conversion induced by parametric amplification. (c) Spectra for the particle and hole components of the system in the laboratory frame, denoted as $(\omega_p/2 \pm \omega)$, respectively. [(d)–(g)] Transmissions (T) measured at the right end (green) in (d) and (f), and at the left end (blue) in (e) and (g). The frequency of the incoming field is $\omega_d > \omega_p/2$ in (d) and (e), and $\omega_d < \omega_p/2$ in (f) and (g). The upper panels of (d) and (e) represent the elastic-scattering components with frequency $\omega_d = (\omega_p/2 + \omega)$, while the lower ones correspond to the inelastic-scattering components with frequency $(\omega_p/2 - \omega)$, and vice versa for (f) and (g). The red dotted curves in (e) and (g) are given by Eqs. (21) and (22). The relevant parameters are $\omega_0 = 2\lambda$, $\lambda = 2t$, $\delta = t/2$, $\kappa_a = 10^{-2}t$, and $\kappa^{(\text{ex})} = t/5$.

V. TOPOLOGICAL AMPLIFICATION AND FREQUENCY CONVERSION

So far, we have discussed the band topology of the 1D photonic lattice and analyzed the edge modes (11) in the squeezed-state representation (6). Upon transforming back into the original basis, the presence of the particle and hole components in these edge modes implies amplification and frequency conversion. To observe these effects, we now shift our focus to the scattering properties of the photonic system, using the input-output formalism. As shown schematically in Fig. 4(a), we couple a waveguide to the left end site to inject the probe field, and two waveguides are coupled to the left and right end sites, respectively, to detect the response of the system to the incoming field. The dynamics of the optical mode at site j is governed by the Langevin equation:

$$\partial_t \hat{a}_j = -i[\hat{a}_j, \hat{H}_{\text{eff}}] - \frac{\kappa_j}{2} \hat{a}_j + \delta_{1,j} \sqrt{\kappa^{(\text{ex})}} \hat{a}_j^{(\text{in})}. \quad (14)$$

Here, $\kappa_j = \kappa_a + (2\delta_{1,j} + \delta_{2N,j})\kappa^{(\text{ex})}$ represents the sum of the intrinsic decay rate κ_a of the optical mode and an additional decay rate $\kappa^{(\text{ex})}$ induced by the coupling of a waveguide to optical mode at site $j = 1, 2N$. The final term in (14) describes the incoming field $\hat{a}_j^{(\text{in})}$ injected through a waveguide. It should be noted that the vacuum fluctuations arising from the environment are negligible compared to the incoming field and can therefore be safely disregarded. For the photonic lattice, the outgoing field $\hat{a}_j^{(\text{out})}$, which leaks out of the mode at site j , can be related to the injected field $\hat{a}_j^{(\text{in})}$ through the input-output relation:

$$\hat{a}_j^{(\text{out})} = \delta_{1,j}\hat{a}_j^{(\text{in})} - \sqrt{\kappa^{(\text{ex})}}\hat{a}_j, \quad (15)$$

where $j = 1, 2N$. By combining this relation with (14), we can derive the transmissions in the frequency domain:

$$T_{ij}^E(\omega) = |\delta_{ij} - i\kappa^{(\text{ex})}G_{ij}^E(\omega)|^2, \quad (16)$$

$$T_{ij}^I(\omega) = \kappa^{(\text{ex})}|G_{ij}^I(\omega)|^2. \quad (17)$$

Equations (16) and (17) represent the probabilities of detecting a photon with frequency $\omega_p/2 \pm \omega$ and $\omega_p/2 \mp \omega$ at site i ($i = 1, 2N$) in the laboratory reference frame, respectively, when a photon with frequency $\omega_p/2 \pm \omega$ is injected into site j . Here, $G_{ij}^{E,I}(\omega)$ are the frequency-domain (retarded) Green's functions that describe elastic and inelastic scatterings from site j to site i , respectively. They are defined by (see Appendix B for details)

$$G_{ij}^E(\omega) = -i \int dt e^{i\omega t} \Theta(t) \langle [\hat{a}_i(t), \hat{a}_j^\dagger(0)] \rangle, \quad (18)$$

$$G_{ij}^I(\omega) = -i \int dt e^{i\omega t} \Theta(t) \langle [\hat{a}_i^\dagger(t), \hat{a}_j^\dagger(0)] \rangle, \quad (19)$$

where $\Theta(t)$ represents the Heaviside step function.

Figures 4(d)–4(g) illustrate the transmissions of the system with nontrivial winding number when injecting a field at frequency $\omega_d = \omega_p/2 + \omega$ in the former two and at frequency $\omega_d = \omega_p/2 - \omega$ in the latter. The elastic-scattering components of the transmission of the incoming field [the upper panels of Figs. 4(d) and 4(e) and lower ones of Figs. 4(f) and 4(g)] are analogous to the signal output of the optical parametric amplifier. Due to the presence of two-photon driving, the transmission undergoes an inelastic-scattering process where the outgoing field has the component with frequency $\omega_p - \omega_d$, as shown in the lower panels of Figs. 4(d) and 4(e) and the upper panels of Figs. 4(f) and 4(g). This inelastic-scattering component corresponds to the idler output of an optical parametric amplifier.

We can quantitatively analyze the inelastic-scattering process for the bulk band [i.e., Figs. 4(d) and 4(f)] by utilizing Eqs. (16)–(19) and neglecting the off-resonance terms. In the regime where $\omega_0, \omega \gg \kappa_j, |\omega - \omega_0|$, we find the following approximations:

$$\tanh^2 \chi T_{ij}^E(\omega) \approx T_{ij}^I(\pm\omega) \approx \coth^2 \chi T_{ij}^E(-\omega), \quad (20)$$

for $i \neq j$. Notably, $T_{ij}^I(\omega) = T_{ij}^I(-\omega)$ holds for $i, j = 1, 2N$. From Eq. (20), in the absence of two-photon driving $\lambda = 0$ (i.e., $\chi = 0$), $T_{ij}^I(\pm\omega)$ vanishes, confirming the origin of the inelastic-scattering process. When the two-photon driving is present, $T_{ij}^I(\pm\omega)$ is proportional to $T_{ij}^E(\pm\omega)$; as the strength of

the two-photon driving λ increases, the ratio either monotonically increases for $\omega_d > \omega_p/2$ or decreases for $\omega_d < \omega_p/2$. The second approximate equality reveals that the transmission of the inelastic-scattering component is greatly amplified (with a ratio of $\coth^2 \chi$ to the signal output) when the incoming field excites the hole band, which is consistent with the observation shown in Fig. 4(f).

Importantly, the transmission from the left end indicates the response of the left edge mode $\hat{\alpha}_L$ to the incoming field and manifests the effect of band topology of the system [see Figs. 4(e) and 4(g)]. For $\delta > 0$ (e.g., $\delta = t/2$ in Figs. 3 and 4), the edge mode appears; the frequencies of its particle and hole components are $\omega_p/2 \pm \tilde{\omega}_0$ in the laboratory frame, respectively. Figure 4(e) shows the emergence of an outgoing field with frequency $\omega_p/2 - \tilde{\omega}_0$ [a peak of $T_{11}^I(-\tilde{\omega}_0)$] when an incoming field with frequency $\omega_p/2 + \tilde{\omega}_0$ is injected into the left end site, corresponding to the phenomenon of frequency down-conversion. Similarly, when the incoming field lies within the hole band gap, a peak appears in the upper panel of Fig. 4(g), indicating a frequency up-conversion. Moreover, in the lower panel, a peak at the elastic-scattering component $T_{11}^E(-\tilde{\omega}_0)$ demonstrates the amplification of the signal beam through the Stokes process, where the signal field is amplified by the parametric down-conversion of the pump field.

The numerical behaviors of topological amplification and frequency down- and up-conversion can also be analyzed. Due to the condition $4\delta \gg \kappa_j, |\omega \pm \tilde{\omega}_0|$, where the edge modes are (almost) isolated from the bulk states by the large gap, the bulk states are far from resonance or off resonance with the incoming field. The influence of bulk states can be safely neglected in the analysis of transmission [i.e., Eqs. (16) and (17)]. In such situation, the system of interest can be reduced to a single-mode system with a two-photon driving and the associated Hamiltonian is obtained by $\hat{H}_{\text{single}} \approx \omega_0 \hat{a}_1^\dagger \hat{a}_1 + \frac{1}{2}\lambda(\hat{a}_1 \hat{a}_1 + \hat{a}_1^\dagger \hat{a}_1^\dagger)$. Thus, we can obtain the transmissions of the elastic- and inelastic-scattering processes as

$$T_{11}^E(\omega) \approx \left| 1 + \kappa^{(\text{ex})} \frac{i(\omega + \omega_0) - \kappa_1/2}{\tilde{\omega}_0^2 - (\omega + i\kappa_1/2)^2} \right|^2 \quad (21)$$

and

$$T_{11}^I(\omega) \approx \frac{(\kappa^{(\text{ex})}\lambda)^2}{|\tilde{\omega}_0^2 - (\omega + i\kappa_1/2)^2|^2}, \quad (22)$$

respectively. The analytical formulas (21) and (22) agree well with the numerical results within the band gap in Figs. 4(e) and 4(g). In the near-resonant limit $\omega \simeq \pm\tilde{\omega}_0$, they can be further simplified, i.e.,

$$T_{11}^E(\pm\tilde{\omega}_0) \approx \frac{(\omega_0 \mp \tilde{\omega}_0)^2}{4\tilde{\omega}_0^2 + \kappa_1^2/4}, \quad T_{11}^I(\pm\tilde{\omega}_0) \approx \frac{\lambda^2}{4\tilde{\omega}_0^2 + \kappa_1^2/4}, \quad (23)$$

for $\omega_0, \tilde{\omega}_0 \gg \kappa_1 \simeq 2\kappa^{(\text{ex})} \gg \kappa_a$. They also show that the topological amplification and frequency conversion become significant as λ increases, while maintaining the condition $4\delta \gg \kappa_1, |\omega \pm \tilde{\omega}_0|$.

We emphasize that these topological phenomena are exclusively observed when the winding number is nonvanishing, corresponding to $\delta > 0$. In Fig. 5, we show the response of the system to the incoming field with frequency $\omega_p/2 \pm \tilde{\omega}_0$ at the left end site. The elastic and inelastic components

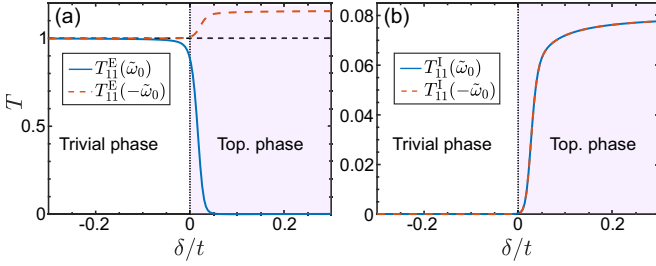


FIG. 5. [(a), (b)] $T_{11}^E(\pm\tilde{\omega}_0)$ in (a) and $T_{11}^I(\pm\tilde{\omega}_0)$ in (b) vs δ . The blue solid (red dashed) curves correspond to the case of the injected beam with frequency $\omega_p/2 + \tilde{\omega}_0$ ($\omega_p/2 - \tilde{\omega}_0$). The transitions occurring at $\delta = 0$ manifest a topological phase transition. The parameters used are the same as those in Fig. 4.

$T_{11}^E(\pm\tilde{\omega}_0)$ and $T_{11}^I(\pm\tilde{\omega}_0)$ manifest a transition at the critical value of hopping strength $\delta = 0$ (i.e., $v = w$). The absence-to-presence transition of amplification and frequency conversion indicates the topological phase transition of the system. Note that $T_{11}^I(\tilde{\omega}_0) = T_{11}^I(-\tilde{\omega}_0)$ as mentioned above.

VI. ROBUSTNESS AGAINST SYMMETRY-PRESERVING DISORDERS

Here we investigate the robustness of topological amplification and frequency conversion against symmetry-preserving disorders, which arises from the topological protection. Specifically, while keeping other parameters unchanged, we introduce the parameter δ_j to Hamiltonian (2) to represent the disorder in the nearest-neighbor hopping of the 1D lattice. This disorder does not break the sublattice symmetry of the system. Here j ($j = 1, 2, \dots, 2N$) denotes the site index. We employ a Bogoliubov transformation on the disordered Hamiltonian, $\hat{\alpha}_j = \cosh \chi \hat{a}_j - e^{i\pi j} \sinh \chi \hat{a}_j$, where $\tanh 2\chi = \lambda/\omega_0$. The transformation allows us to obtain

$$\tilde{H} = \sum_{j=1}^{2N} [\tilde{\omega}_0 \hat{\alpha}_j^\dagger \hat{\alpha}_j + (t + e^{i\pi j} \delta_j) (\hat{\alpha}_j^\dagger \hat{\alpha}_{j+1} + \text{H.c.})]. \quad (24)$$

Then the edge modes can be constructed as

$$\tilde{\alpha}_L = \sum_{n=1}^N \mu_n^{n-1} \hat{\alpha}_{2n-1}, \quad \tilde{\alpha}_R = \sum_{n=1}^N \nu_{N-n+1}^{N-n} \hat{\alpha}_{2n}, \quad (25)$$

where the coefficients are given by

$$\mu_n^{n-1} = \prod_{l=1}^{j-1} \frac{\delta_{2l-1} - t}{\delta_{2l} + t}, \quad \nu_{N-n+1}^{N-n} = \frac{\mu_N^{N-1}}{\mu_n^{n-1}}.$$

Note that the existence of edge modes requires the condition $|(t - \delta_{2n-1})/(t + \delta_{2n})| < 1$ to be satisfied. The commutation relations can be readily verified as follows:

$$\begin{aligned} [\tilde{\alpha}_L, \tilde{H}] &= \tilde{\omega}_0 \tilde{\alpha}_L + O(\mu_N^{N-1}), \\ [\tilde{\alpha}_R, \tilde{H}] &= \tilde{\omega}_0 \tilde{\alpha}_R + O(\nu_1^{N-1}). \end{aligned} \quad (26)$$

These quantities are (almost) conserved when N is sufficiently large. It implies that the edge modes for the disordered system are robust against symmetry-preserving disorders due to the topological protection.

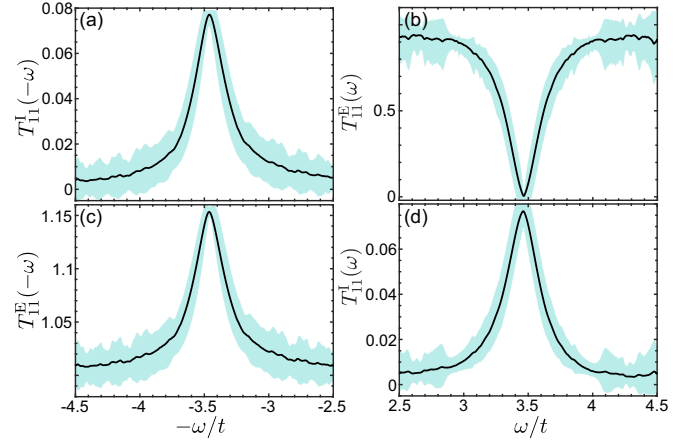


FIG. 6. (a) $T_{11}^I(-\omega)$ and (c) $T_{11}^E(-\omega)$ for $-\omega < 0$, and (b) $T_{11}^E(\omega)$ and (d) $T_{11}^I(\omega)$ for $\omega > 0$ are shown. In (a) and (b) the frequency of the incoming field ω_d exceeds $\omega_p/2$, while in (c) and (d) $\omega_d < \omega_p/2$. The shaded region represents the standard deviation of $T_{11}^{E/I}$ across 100 samples, while the black curve represents their average value. The strength of disorders is set as $D = t/2$. Other parameters remain the same as Fig. 4.

The edge modes in the disordered system imply the existence of topological amplification and frequency conversion and they would also exhibit robustness against symmetry-preserving disorder. To see this, we consider a set of 100 samples that maintain sublattice symmetry. The disorder strength defined by $D = \max\{\Delta\delta_j\}$ with $\Delta\delta_j = |\delta_j - \delta|$ is assumed as $t/2$. We calculate the transmissions of the left end site, which encompass both elastic- and inelastic-scattering processes, denoted as $T_{11}^E(\pm\omega)$ and $T_{11}^I(\pm\omega)$, respectively. In Fig. 6, the shaded region represents the standard deviation of these samples, while the black curve corresponds to their average value. It is evident that the topological amplification and frequency conversion remain robust to this type of disorder. This is because this disordered system can still be treated as a single-mode system with a two-photon driving under the condition $4\delta_j \gg \kappa_j, |\omega \pm \tilde{\omega}_0|$, as discussed in Sec. V. Within the input-output formalism, the elastic- and inelastic-scattering components are approximately equivalent to Eqs. (21) and (22), respectively.

In addition, as discussed in Sec. IV, the system of interest is topologically equivalent to the bare SSH model in terms of the Bloch band. In the presence of disorder, the condition for the existence of edge modes, i.e., $|(t - \delta_{2n-1})/(t + \delta_{2n})| < 1$, holds true for both systems, according to the bulk-edge correspondence. The edge modes of the bare SSH model explicitly follow the formulas in Eq. (25) with replacements $\tilde{\alpha}_{L/R} \rightarrow \hat{a}_{L/R}$ and $\hat{\alpha}_j \rightarrow \hat{a}_j$ ($j = 2n - 1, 2n$). This implies that their edge modes will disappear (appear) simultaneously, while accompanied by the disappearance (appearance) of amplification and frequency conversion in our system. Therefore, these two systems exhibit similar robustness against symmetry-preserving disorders in terms of their edge modes.

VII. EXPERIMENTAL REALIZATION

The proposed system can be realized in various quantum-optic setups, including photonic crystal coupled cavity arrays

[56] fabricated using nonlinear materials with $\chi^{(2)}$ susceptibility [57–59], as well as superconducting microwave circuits with coupled resonators [60–63]. In implementation, it is crucial to generate parametric gain (i.e., two-photon driving) with a specific relative phase in the Hamiltonian. The parametric gain can be achieved through three-wave mixing processes, which arise from the optical nonlinear effect. One effective approach to engineer such processes is by utilizing the Josephson-junction-based superconducting nonlinear asymmetric inductive element (SNAIL) parametric amplifier (SPA) [62].

In a SNAIL device located at site j , the Hamiltonian can be described up to the third order as

$$\hat{H}_{\text{SPA}} = \omega_a \hat{a}_j^\dagger \hat{a}_j + \omega_b \hat{b}_j^\dagger \hat{b}_j + g_3 (\hat{a}_j + \hat{a}_j^\dagger)^2 (\hat{b}_j + \hat{b}_j^\dagger), \quad (27)$$

where \hat{a}_j and \hat{b}_j represent the annihilation operators of harmonic oscillators with resonant frequencies ω_a and ω_b (approximately equal to $2\omega_a$), respectively. The parameter $g_3 \in \mathbb{R}$ denotes the interaction strength of the third-order nonlinearity. We note that g_3 is equivalent to G defined in Sec. II. These terms in Eq. (27) can be adjusted *in situ* by controlling the applied magnetic flux Φ through the array of the SNAIL loop. To enable parametric amplification, a strong microwave tone at $\omega_p \simeq \omega_b$ can be applied to generate an intracavity field $\langle \hat{b}_j \rangle = \beta_j \in \mathbb{C}$. As a result, terms $\hat{a}_j^\dagger \hat{a}_j^\dagger$ and $\hat{a}_j \hat{a}_j$ exhibit (near) resonance. By engineering the phase of β_j using the pump field, we can obtain the desired squeezing term $g_3 \beta_j \hat{a}_j^\dagger \hat{a}_j^\dagger + \text{H.c.}$, which has the relative phase ϕ within a unit cell.

The magnitude of the parametric-gain strength $g_3 \beta_j = \lambda_j/2$ utilized in the above can be achieved through careful engineering of the SPA device and the pump field. Generally, the normal hopping strength is much smaller compared to the resonant frequency, for example, $t_{1,2} \approx 10^{-2} \omega_a$ as reported in Ref. [61]. On the other hand, the third-order nonlinear interaction strength is given by $g_3/2\pi \approx 0.3\text{--}30$ MHz and the resonant frequency is $\omega_a/2\pi \approx 6\text{--}7.84$ GHz, as shown in Ref. [62]. With the mean photon number of the intracavity field \bar{n} ($\bar{n} = |\beta_j|^2$) reaching hundreds or thousands ($\bar{n} \approx 10^2\text{--}10^3$), we can achieve the desired parameter regime where the parametric-gain strength becomes comparable to the hopping rates, i.e., $t_{1,2} \sim g_3 \sqrt{\bar{n}}$.

An alternative approach to generate optical parametric gain is through the optomechanical interaction in photonic crystals [64,65]. By illuminating light on the photonic lattice and adiabatically eliminating the mechanical component, one can finally achieve the desired parametric gain terms. Notably, a dimer chain consisting of optomechanical crystal arrays has been reported in Ref. [75], indicating the feasibility of implementing our proposed dimer chain in this platform. This approach offers an additional avenue for experimental realization and further validates the potential applicability of our model in different experimental settings.

VIII. DISCUSSION

In the field of topological nonlinear photonics [76], several recent works are highly relevant to the findings presented in this paper.

First, it has been demonstrated that the Kerr nonlinearity preserving $U(1)$ symmetry can be used to achieve topological amplification and subsequent high-harmonic generation [77–80]. In contrast, to realize such an amplification, we utilize the stronger $\chi^{(2)}$ nonlinearity which breaks the $U(1)$ symmetry. Our paper also demonstrates both topological frequency down- and up-conversion, respectively, where the frequency of the outgoing field is lower and higher than that of the incoming field, as illustrated in Figs. 4(e) and 4(g). As a further distinction to the prior works, our research offers a notable advantage in terms of flexible tuning of topological amplification and frequency conversion. This is achieved by injecting the pump and probe fields into a single site, either the left or right end site. The tunability holds promise for various applications, including topological transducers, modulators, switches, etc.

Furthermore, an alternative approach to achieve topological amplification involves accessing the dynamical-instability regime [36,55,81,82]. The eigenvalues of the boundary or edge modes are complex ($E \in \mathbb{C}$), exhibiting exponential growth, while the bulk states remain dynamically stable. This approach differs significantly from the scenario described in the present paper since our system is stable.

In addition, it is noteworthy that directional amplification can occur in driven-dissipative photonic systems [83–85], which is fundamentally related to non-Hermitian point-gap or spectral topology [86,87]. This nontrivial topology arises due to the complex-valued spectrum winding around a reference energy point in the complex plane. Note that the parametric amplifier can also induce the nontrivial point-gap topology in a Hermitian system [88]. In contrast, the system of interest possesses real energies in both stability regimes. Its band topology falls within the Hermitian framework and relies on the wave function of the system (see Appendix A), rather than its spectrum. This distinction arises because the real spectrum of our system does not form a closed loop in the complex plane, resulting in a trivial topological number. Hence, the amplification of edge states discussed in this paper is completely distinct from the phenomena observed in these previous works.

IX. CONCLUSION

In conclusion, we have investigated the 1D photonic lattice with $\chi^{(2)}$ nonlinear interaction, specifically focusing on a dimer chain subject to two-photon driving. The critical behavior of the transition has been analyzed from thermodynamic and dynamical stability to instability in the system. We have examined the impact of the two-photon driving on closing the topological gap and the emergence of edge modes through the bulk-edge correspondence. Moreover, we have demonstrated the topological amplification and frequency conversion using the input-output formalism, which exhibit an absence-to-presence transition at a critical hopping strength. These topological phenomena are robust against symmetry-preserving disorders. The proposed model can be experimentally realized in various quantum-optics platforms. Our paper holds potential for the engineering of topological quantum-optics devices with excellent fault-tolerance properties.

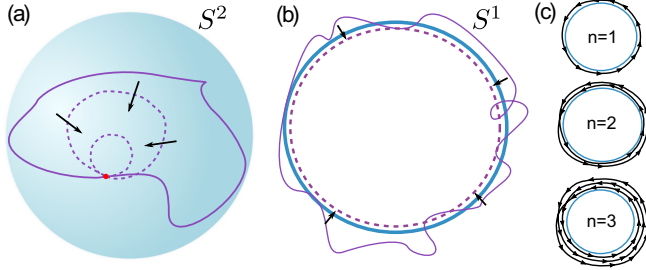


FIG. 7. [(a), (b)] Schematics of the homotopy of the mappings $S^1 \rightarrow S^2$ (a) and $S^1 \rightarrow S^1$ (b). (a) The circle (one-sphere) can be continuously deformed to the red point on the two-sphere. (b) The continuous deformation of $S^1 \rightarrow S^1$. The black arrows depict the deformation in (a) and (b). (c) Three elements of the homotopy group $\pi_1(S^1) \cong \mathbb{Z}$, $n = 1, 2, 3$, represent three nontrivial windings around the circle. The arrows denote the orientation of the windings.

ACKNOWLEDGMENTS

We thank Wen Huang and Gui-Lei Zhu for their critical reading of this paper. This work is supported by the National Key Research and Development Program of China (Grant No. 2021YFA1400702) and the National Natural Science Foundation of China (Grants No. 11875029, No. 12147143, and No. 11975103).

APPENDIX A: TOPOLOGY FOR 1D LATTICES WITH CHIRAL SYMMETRY

According to the Altland-Zirnbauer classification [52], the chiral symmetry protects the topology in a 1D noninteracting and particle-number-conserving system. To illustrate this, let us consider a 1D two-band model with the Bloch Hamiltonian denoted as

$$H(k) = \mathbf{h}(k) \cdot \boldsymbol{\sigma}, \quad (\text{A1})$$

where the vector $\mathbf{h}(k) = (h_x(k), h_y(k), h_z(k))$ with $k \in [-\pi, \pi)$ describes the dispersion of the model, and $\boldsymbol{\sigma} = (\sigma_x, \sigma_y, \sigma_z)$ refers to the Pauli matrices. In the absence of chiral symmetry, the eigenstate for the upper band can be expressed as

$$u(k) = \left(\sin \frac{\theta(k)}{2}, \cos \frac{\theta(k)}{2} e^{i\varphi(k)} \right)^T \quad (\text{A2})$$

where $\theta(k) = 2 \arctan \sqrt{(h_x + h_z)/(h_x - h_z)}$, $\varphi(k) = \arctan(h_y/h_x)$, and $h = \sqrt{h_x^2 + h_y^2 + h_z^2}$. Equation (A2) reveals that $u(k)$ is equivalent to the Bloch sphere (the two-sphere denoted by S^2) when θ runs over $[0, \pi]$ and φ runs over $[-\pi, \pi)$ for $k \in [-\pi, \pi)$. It is worth noting that the 1D Brillouin zone is equivalent to the one-sphere denoted by S^1 . Therefore, we establish a continuous mapping $u(k) : S^1 \rightarrow S^2$, $k \mapsto u(k)$. Generally, the topological number characterizes the ways of continuous mapping from S^1 to S^2 , which can be summarized by the homotopy group. It is *always* possible to continuously deform S^1 to a point on S^2 , as depicted in Fig. 7(a). Equivalently, the homotopy group of the mapping $S^1 \rightarrow S^2$ is trivial.

However, the scenario is markedly different in the presence of chiral symmetry, where $\Gamma H(k) \Gamma^{-1} = -H(k)$, with $\Gamma = \sigma_z$ being an example. Here the chiral symmetry is mathematically equivalent to the sublattice symmetry in the system of interest. In this case, the eigenstate takes the form

$$u(k) = \frac{1}{\sqrt{2}} (1, e^{i\varphi(k)})^T. \quad (\text{A3})$$

Unlike Eq. (A2), the phase $\theta(k)$ becomes fixed. The eigenstate (A3) is then isomorphic to S^1 and represents a continuous mapping $u(k) : S^1 \rightarrow S^1$, which can be visualized as a circle wrapped by another circle, as depicted in Figs. 7(b) and 7(c). Intuitively, the winding of the circle describes the first simply connected homotopy group denoted by $\pi_1(S^1)$, which is isomorphic to the set of integers, i.e., $\pi_1(S^1) \cong \mathbb{Z}$. This can be characterized by the winding number (8). In Fig. 7(c), the three mappings, i.e., $\varphi(k) = nk$ with $n = 1, 2, 3$, correspond to the winding number of a loop around the origin in the plane. It is important to note that the counterclockwise orientation for the winding has been selected as the forward direction. Subsequently, one can also employ the auxiliary space depicted in Fig. 3(a) to visualize the band topology in the presence of chiral symmetry.

APPENDIX B: SCATTERING THEORY FOR QUADRATIC-BOSONIC SYSTEMS

1. Green's function

Now we consider a general bosonic system with a particle-number-nonconserving term, described by the Hamiltonian $\hat{H}_G = \frac{1}{2} \hat{\Phi}^\dagger H_G \hat{\Phi}$. Here $\hat{\Phi} = (\hat{a}_1, \dots, \hat{a}_M, \hat{a}_1^\dagger, \dots, \hat{a}_M^\dagger)^T$ represents the Nambu spinor. The first-quantized Hamiltonian satisfies the particle-hole symmetry:

$$\tau_x H_G^* \tau_x = H_G, \quad (\text{B1})$$

where $\tau_x = \sigma_x \otimes I_M$. For the Nambu spinor, the retarded Green's function is defined as

$$\begin{aligned} G_{R,ij}(t, t') &= -i\Theta(t - t') \langle [\hat{\Phi}_i(t), \hat{\Phi}_j^\dagger(t')] \rangle = -i\Theta(t - t') \\ &\times \begin{pmatrix} \langle [\hat{a}_i(t), \hat{a}_j^\dagger(t')] \rangle & \langle [\hat{a}_i(t), \hat{a}_j(t')] \rangle \\ \langle [\hat{a}_i^\dagger(t), \hat{a}_j^\dagger(t')] \rangle & \langle [\hat{a}_i^\dagger(t), \hat{a}_j(t')] \rangle \end{pmatrix} \\ &= \begin{pmatrix} G_{R,ij}^E(t, t') & [G_{R,ij}^I(t, t')]^* \\ G_{R,ij}^I(t, t') & G_{A,ji}^E(t', t) \end{pmatrix}, \end{aligned} \quad (\text{B2})$$

where the subscripts R and A denote the retarded and advanced Green's functions, respectively. In the steady-state regime, the Green's function can be transformed to the frequency domain as

$$G_{R,ij}(\omega) = \begin{pmatrix} G_{R,ij}^E(\omega) & [G_{R,ij}^I(-\omega)]^* \\ G_{R,ij}^I(\omega) & [G_{R,ij}^E(-\omega)]^* \end{pmatrix}. \quad (\text{B3})$$

Here, we have used the identity $G_A(\omega) = [G_R(\omega)]^\dagger$. In matrix form, the Green's function can be expressed as

$$G_R(\omega) = \left(\omega \tau_z - H_G + \frac{i}{2} \kappa \tau_z \right)^{-1} \equiv \begin{pmatrix} G^E(\omega) & [G^I(-\omega)]^* \\ G^I(\omega) & [G^E(-\omega)]^* \end{pmatrix}, \quad (\text{B4})$$

where the uniform decay rate κ is taken into account. From now on, we omit the subscript R since it does not cause any confusion.

Now let us analyze the elastic and inelastic components in (B4). The Hamiltonian H_G can be diagonalized by the pseudounitary transformation K [67,68], i.e., $K^\dagger H_G K = \begin{pmatrix} E & \\ & E \end{pmatrix}$, where $E = \text{diag}(E_1, \dots, E_M)$ represents the energy of the system, and $K^\dagger \tau_z K = \tau_z$ with $\tau_z = \text{diag}(I_M, -I_M)$. Due to the particle-hole symmetry (B1), the transformation takes the form $K = \begin{pmatrix} U & V^* \\ V & U^* \end{pmatrix}$. Substituting K back into Eq. (B4), the elastic and inelastic components are given by

$$G^E(\omega) = U \left(\omega I - E + \frac{i}{2} \kappa I \right)^{-1} U^\dagger - V^* \left(\omega I + E + \frac{i}{2} \kappa I \right)^{-1} V^T, \quad (\text{B5})$$

$$G^I(\omega) = V \left(\omega I - E + \frac{i}{2} \kappa I \right)^{-1} U^\dagger - U^* \left(\omega I + E + \frac{i}{2} \kappa I \right)^{-1} V^T, \quad (\text{B6})$$

respectively.

2. Scattering matrix

The Langevin equation for the general quadratic-bosonic system is given in the frequency domain by

$$\left(\omega - \tau_z H_G + i \frac{\kappa}{2} \right) \hat{\Phi}[\omega] = i \sqrt{\kappa} \hat{\Phi}^{(\text{in})}[\omega]. \quad (\text{B7})$$

Here, we neglect the external decay. Combining it with the input-output relation $\hat{\Phi}^{\text{out}} = \hat{\Phi}^{\text{in}} - \sqrt{\kappa} \hat{\Phi}$, we arrive at $\hat{\Phi}^{\text{out}}[\omega] = S(\omega) \hat{\Phi}^{\text{in}}[\omega]$, where the scattering matrix $S(\omega)$ is given by

$$\begin{aligned} S(\omega) &= I - i \kappa G(\omega) \tau_z = \begin{pmatrix} I - i \kappa G^E(\omega) & -i \kappa [G^I(-\omega)]^* \\ -i \kappa G^I(\omega) & I - i \kappa [G^E(-\omega)]^* \end{pmatrix} \\ &\equiv \begin{pmatrix} S^E(\omega) & [S^I(-\omega)]^* \\ S^I(\omega) & [S^E(-\omega)]^* \end{pmatrix}. \end{aligned} \quad (\text{B8})$$

The elastic- and inelastic-scattering processes are determined by $S^E(\omega)$ and $S^I(\omega)$, respectively. Using the Kubo formula, we can obtain the elastic and inelastic transmissions as given in Eqs. (16) and (17) in the main text.

-
- [1] F. D. M. Haldane and S. Raghu, Possible Realization of Directional Optical Waveguides in Photonic Crystals with Broken Time-Reversal Symmetry, *Phys. Rev. Lett.* **100**, 013904 (2008).
 - [2] Z. Wang, Y. D. Chong, J. D. Joannopoulos, and M. Soljačić, Reflection-Free One-Way Edge Modes in a Gyromagnetic Photonic Crystal, *Phys. Rev. Lett.* **100**, 013905 (2008).
 - [3] Z. Wang, Y. Chong, J. D. Joannopoulos, and M. Soljačić, Observation of unidirectional backscattering-immune topological electromagnetic states, *Nature (London)* **461**, 772 (2009).
 - [4] S. A. Skirlo, L. Lu, and M. Soljačić, Multimode One-Way Waveguides of Large Chern Numbers, *Phys. Rev. Lett.* **113**, 113904 (2014).
 - [5] S. A. Skirlo, L. Lu, Y. Igarashi, Q. Yan, J. Joannopoulos, and M. Soljačić, Experimental Observation of Large Chern Numbers in Photonic Crystals, *Phys. Rev. Lett.* **115**, 253901 (2015).
 - [6] W.-J. Chen, S.-J. Jiang, X.-D. Chen, B. Zhu, L. Zhou, J.-W. Dong, and C. T. Chan, Experimental realization of photonic topological insulator in a uniaxial metacrystal waveguide, *Nat. Commun.* **5**, 5782 (2014).
 - [7] X. Cheng, C. Jouvaud, X. Ni, S. H. Mousavi, A. Z. Genack, and A. B. Khanikaev, Robust reconfigurable electromagnetic pathways within a photonic topological insulator, *Nat. Mater.* **15**, 542 (2016).
 - [8] S. Barik, A. Karasahin, C. Flower, T. Cai, H. Miyake, W. DeGottardi, M. Hafezi, and E. Waks, A topological quantum optics interface, *Science* **359**, 666 (2018).
 - [9] M. Hafezi, E. A. Demler, M. D. Lukin, and J. M. Taylor, Robust optical delay lines with topological protection, *Nat. Phys.* **7**, 907 (2011).
 - [10] A. B. Khanikaev, S. Hossein Mousavi, W.-K. Tse, M. Kargarian, A. H. MacDonald, and G. Shvets, Photonic topological insulators, *Nat. Mater.* **12**, 233 (2013).
 - [11] L.-H. Wu and X. Hu, Scheme for Achieving a Topological Photonic Crystal by Using Dielectric Material, *Phys. Rev. Lett.* **114**, 223901 (2015).
 - [12] A. V. Nalitov, G. Malpuech, H. Terças, and D. D. Solnyshkov, Spin-Orbit Coupling and the Optical Spin Hall Effect in Photonic Graphene, *Phys. Rev. Lett.* **114**, 026803 (2015).
 - [13] K. Y. Bliokh, F. J. Rodríguez-Fortuño, F. Nori, and A. V. Zayats, Spin-orbit interactions of light, *Nat. Photon.* **9**, 796 (2015).
 - [14] Y. Yang, Y. F. Xu, T. Xu, H.-X. Wang, J.-H. Jiang, X. Hu, and Z. H. Hang, Visualization of a Unidirectional Electromagnetic Waveguide Using Topological Photonic Crystals Made of Dielectric Materials, *Phys. Rev. Lett.* **120**, 217401 (2018).
 - [15] M. C. Rechtsman, J. M. Zeuner, Y. Plotnik, Y. Lumer, D. Podolsky, F. Dreisow, S. Nolte, M. Segev, and A. Szameit, Photonic Floquet topological insulators, *Nature (London)* **496**, 196 (2013).
 - [16] G. Jotzu, M. Messer, R. Desbuquois, M. Lebrat, T. Uehlinger, D. Greif, and T. Esslinger, Experimental realization of the topological Haldane model with ultracold fermions, *Nature (London)* **515**, 237 (2014).
 - [17] L. Lu, J. D. Joannopoulos, and M. Soljačić, Topological photonics, *Nat. Photon.* **8**, 821 (2014).
 - [18] A. B. Khanikaev and G. Shvets, Two-dimensional topological photonics, *Nat. Photon.* **11**, 763 (2017).
 - [19] X.-C. Sun, C. He, X.-P. Liu, M.-H. Lu, S.-N. Zhu, and Y.-F. Chen, Two-dimensional topological photonic systems, *Prog. Quant. Electron.* **55**, 52 (2017).
 - [20] T. Ozawa, H. M. Price, A. Amo, N. Goldman, M. Hafezi, L. Lu, M. C. Rechtsman, D. Schuster, J. Simon, O. Zilberberg, and I. Carusotto, Topological photonics, *Rev. Mod. Phys.* **91**, 015006 (2019).
 - [21] R. Shindou, R. Matsumoto, S. Murakami, and J.-ichiro Ohe, Topological chiral magnonic edge mode in a magnonic crystal, *Phys. Rev. B* **87**, 174427 (2013).
 - [22] G. Engelhardt and T. Brandes, Topological bogoliubov excitations in inversion-symmetric systems of interacting bosons, *Phys. Rev. A* **91**, 053621 (2015).

- [23] C.-E. Bardyn, T. Karzig, G. Refael, and T. C. H. Liew, Chiral Bogoliubov excitations in nonlinear bosonic systems, *Phys. Rev. B* **93**, 020502(R) (2016).
- [24] V. Peano, M. Houde, C. Brendel, F. Marquardt, and A. A. Clerk, Topological phase transitions and chiral inelastic transport induced by the squeezing of light, *Nat. Commun.* **7**, 10779 (2016).
- [25] Z.-F. Xu, L. You, A. Hemmerich, and W. V. Liu, π -Flux Dirac Bosons and Topological Edge Excitations in a Bosonic Chiral p -Wave Superfluid, *Phys. Rev. Lett.* **117**, 085301 (2016).
- [26] V. Peano, M. Houde, F. Marquardt, and A. A. Clerk, Topological Quantum Fluctuations and Traveling Wave Amplifiers, *Phys. Rev. X* **6**, 041026 (2016).
- [27] M. Di Liberto, A. Hemmerich, and C. Morais Smith, Topological Varma Superfluid in Optical Lattices, *Phys. Rev. Lett.* **117**, 163001 (2016).
- [28] X. Zhou, Y. Wang, D. Leykam, and Y. D. Chong, Optical isolation with nonlinear topological photonics, *New J. Phys.* **19**, 095002 (2017).
- [29] D. A. Dobrykh, A. V. Yulin, A. P. Slobozhanyuk, A. N. Poddubny, and Yu. S. Kivshar, Nonlinear Control of Electromagnetic Topological Edge States, *Phys. Rev. Lett.* **121**, 163901 (2018).
- [30] B. Midya, H. Zhao, and L. Feng, Non-Hermitian photonics promises exceptional topology of light, *Nat. Commun.* **9**, 2674 (2018).
- [31] G.-Q. Luo, A. Hemmerich, and Z.-F. Xu, Bosonic topological excitations from the instability of a quadratic band crossing, *Phys. Rev. A* **98**, 053617 (2018).
- [32] T. Goren, K. Plekhanov, F. Appas, and K. Le Hur, Topological Zak phase in strongly coupled LC circuits, *Phys. Rev. B* **97**, 041106(R) (2018).
- [33] A. McDonald, T. Pereg-Barnea, and A. A. Clerk, Phase-Dependent Chiral Transport and Effective Non-Hermitian Dynamics in a Bosonic Kitaev-Majorana Chain, *Phys. Rev. X* **8**, 041031 (2018).
- [34] R. Chaunsali and G. Theocharis, Self-induced topological transition in phononic crystals by nonlinearity management, *Phys. Rev. B* **100**, 014302 (2019).
- [35] S. A. Díaz, J. Klinovaja, and D. Loss, Topological Magnons and Edge States in Antiferromagnetic Skyrmion Crystals, *Phys. Rev. Lett.* **122**, 187203 (2019).
- [36] D. Malz, J. Knolle, and A. Nunnenkamp, Topological magnon amplification, *Nat. Commun.* **10**, 3937 (2019).
- [37] D. Porras and S. Fernández-Lorenzo, Topological Amplification in Photonic Lattices, *Phys. Rev. Lett.* **122**, 143901 (2019).
- [38] H. Kondo, Y. Akagi, and H. Katsura, \mathbb{Z}_2 topological invariant for magnon spin Hall systems, *Phys. Rev. B* **99**, 041110(R) (2019).
- [39] H. Kondo, Y. Akagi, and H. Katsura, Three-dimensional topological magnon systems, *Phys. Rev. B* **100**, 144401 (2019).
- [40] V. P. Flynn, E. Cobanera, and L. Viola, Topology by Dissipation: Majorana Bosons in Metastable Quadratic Markovian Dynamics, *Phys. Rev. Lett.* **127**, 245701 (2021).
- [41] X.-Q. Wang, G.-Q. Luo, J.-Yu. Liu, W. V. Liu, A. Hemmerich, and Z.-F. Xu, Evidence for an atomic chiral superfluid with topological excitations, *Nature (London)* **596**, 227 (2021).
- [42] D. Leykam, E. Smolina, A. Maluckov, S. Flach, and D. A. Smirnova, Probing Band Topology Using Modulational Instability, *Phys. Rev. Lett.* **126**, 073901 (2021).
- [43] H. Nasari, G. G. Pyrialakos, D. N. Christodoulides, and M. Khajavikhan, Non-Hermitian topological photonics, *Opt. Mater. Express* **13**, 870 (2023).
- [44] J. P. Blaizot and G. Ripka, *Quantum Theory of Finite Systems* (MIT, Cambridge, MA, 1986).
- [45] G. E. Volovik, *The Universe in a Helium Droplet* (Oxford University, New York, 2003).
- [46] V. Gurarie and J. T. Chalker, Some Generic Aspects of Bosonic Excitations in Disordered Systems, *Phys. Rev. Lett.* **89**, 136801 (2002).
- [47] F. Lu and Y.-M. Lu, Magnon band topology in spin-orbital coupled magnets: Classification and application to $\alpha - \text{RuCl}_3$, [arXiv:1807.05232](https://arxiv.org/abs/1807.05232).
- [48] K. Kawabata, K. Shiozaki, M. Ueda, and M. Sato, Symmetry and Topology in Non-Hermitian Physics, *Phys. Rev. X* **9**, 041015 (2019).
- [49] M. Lein and K. Sato, Krein-Schrödinger formalism of bosonic Bogoliubov-de Gennes and certain classical systems and their topological classification, *Phys. Rev. B* **100**, 075414 (2019).
- [50] Z. Zhou, L.-L. Wan, and Z.-F. Xu, Topological classification of excitations in quadratic bosonic systems, *J. Phys. A* **53**, 425203 (2020).
- [51] Q.-Ru. Xu, V. P. Flynn, A. Alase, E. Cobanera, L. Viola, and G. Ortiz, Squaring the fermion: The threefold way and the fate of zero modes, *Phys. Rev. B* **102**, 125127 (2020).
- [52] C.-K. Chiu, J. C. Y. Teo, A. P. Schnyder, and S. Ryu, Classification of topological quantum matter with symmetries, *Rev. Mod. Phys.* **88**, 035005 (2016).
- [53] M. O. Scully and M. S. Zubairy, *Quantum Optics* (Cambridge University, New York, 1997).
- [54] L.-L. Wan, Z. Zhou, and Z.-F. Xu, Squeezing-induced topological gap opening on bosonic Bogoliubov excitations, *Phys. Rev. A* **103**, 013308 (2021).
- [55] R. Barnett, Edge-state instabilities of bosons in a topological band, *Phys. Rev. A* **88**, 063631 (2013).
- [56] M. Notomi, E. Kuramochi, and T. Tanabe, Large-scale arrays of ultrahigh-Q coupled nanocavities, *Nat. Photon.* **2**, 741 (2008).
- [57] S. Mookherjea and A. Yariv, Coupled resonator optical waveguides, *IEEE J. Sel. Topics Quantum Electron.* **8**, 448 (2002).
- [58] B. J. Eggleton, B. Luther-Davies, and K. Richardson, Chalcogenide photonics, *Nat. Photon.* **5**, 141 (2011).
- [59] J. Dahdah, M. Pilar-Bernal, N. Courjal, G. Ulliac, and F. Baida, Near-field observations of light confinement in a two dimensional lithium niobate photonic crystal cavity, *J. Appl. Phys.* **110**, 074318 (2011).
- [60] J. Ningyuan, C. Owens, A. Sommer, D. Schuster, and J. Simon, Time- and Site-Resolved Dynamics in a Topological Circuit, *Phys. Rev. X* **5**, 021031 (2015).
- [61] M. Fitzpatrick, N. M. Sundaresan, A. C. Y. Li, J. Koch, and A. A. Houck, Observation of a Dissipative Phase Transition in a One-Dimensional Circuit QED Lattice, *Phys. Rev. X* **7**, 011016 (2017).
- [62] N. E. Frattini, V. V. Sivak, A. Lingenfelter, S. Shankar, and M. H. Devoret, Optimizing the Nonlinearity and Dissipation of a SNAIL Parametric Amplifier for Dynamic Range, *Phys. Rev. Appl.* **10**, 054020 (2018).
- [63] C. S. Wang, J. C. Curtis, B. J. Lester, Y. Zhang, Y. Y. Gao, J. Freeze, V. S. Batista, P. H. Vaccaro, I. L. Chuang, L. Frunzio, L. Jiang, S. M. Girvin, and R. J. Schoelkopf, Efficient Multiphoton

- Sampling of Molecular Vibronic Spectra on a Superconducting Bosonic Processor, *Phys. Rev. X* **10**, 021060 (2020).
- [64] A. H. Safavi-Naeini, S. Gröblacher, J. T. Hill, J. Chan, M. Aspelmeyer, and O. Painter, Squeezed light from a silicon micromechanical resonator, *Nature (London)* **500**, 185 (2013).
- [65] J. del Pino, J. J. Slim, and E. Verhagen, Non-hermitian chiral phononics through optomechanically induced squeezing, *Nature (London)* **606**, 82 (2022).
- [66] D. Englund, I. Fushman, and J. Vuckovic, General recipe for designing photonic crystal cavities, *Opt. Express* **13**, 5961 (2005).
- [67] J. H. P. Colpa, Diagonalization of the quadratic boson hamiltonian with zero modes: II. Physical, *Physica A* **134**, 417 (1986).
- [68] R. Simon, S. Chaturvedi, and V. Srinivasan, Congruences and canonical forms for a positive matrix: Application to the Schweinler-Wigner extremum principle, *J. Math. Phys.* **40**, 3632 (1999).
- [69] T. Kapitula and K. Promislow, *Spectral and Dynamical Stability of Nonlinear Waves* (Springer, New York, 2013).
- [70] Y. Kawaguchi and M. Ueda, Spinor Bose-Einstein condensates, *Phys. Rep.* **520**, 253 (2012).
- [71] W. D. Heiss, The physics of exceptional points, *J. Phys. A* **45**, 444016 (2012).
- [72] C. Chan, L. Zhang, T. F. Jeffrey Poon, Y.-P. He, Y.-Qi. Wang, and X.-J. Liu, Generic Theory for Majorana Zero Modes in 2D Superconductors, *Phys. Rev. Lett.* **119**, 047001 (2017).
- [73] Y. Hadad, A. B. Khanikaev, and A. Alù, Self-induced topological transitions and edge states supported by nonlinear staggered potentials, *Phys. Rev. B* **93**, 155112 (2016).
- [74] S. Lieu, Topological symmetry classes for non-Hermitian models and connections to the bosonic Bogoliubov–de Gennes equation, *Phys. Rev. B* **98**, 115135 (2018).
- [75] F. Zangeneh-Nejad and R. Fleury, Topological optomechanically induced transparency, *Opt. Lett.* **45**, 5966 (2020).
- [76] D. Smirnova, D. Leykam, Y. Chong, and Y. Kivshar, Nonlinear topological photonics, *Appl. Phys. Rev.* **7**, 021306 (2020).
- [77] S. Kruk, A. Poddubny, D. Smirnova, L. Wang, A. Slobozhanyuk, A. Shorokhov, I. Kravchenko, B. Luther-Davies, and Y. Kivshar, Nonlinear light generation in topological nanostructures, *Nat. Nanotechnol.* **14**, 126 (2019).
- [78] Z. Lan, J. W. You, and N. C. Panoiu, Nonlinear one-way edge-mode interactions for frequency mixing in topological photonic crystals, *Phys. Rev. B* **101**, 155422 (2020).
- [79] S. S. Kruk, W. Gao, D.-Y. Choi, T. Zentgraf, S. Zhang, and Y. Kivshar, Nonlinear imaging of nanoscale topological corner states, *Nano Lett.* **21**, 4592 (2021).
- [80] B.-Uk. Sohn, Y.-X. Huang, Ju. W. Choi, G. F. R. Chen, D. K. T. Ng, S. A. Yang, and D. T. H. Tan, A topological nonlinear parametric amplifier, *Nat. Commun.* **13**, 7218 (2022).
- [81] I. Septembre, S. Koniakhin, J. S. Meyer, D. D. Solnyshkov, and G. Malpuech, Parametric amplification of topological interface states in synthetic Andreev bands, *Phys. Rev. B* **103**, 214504 (2021).
- [82] A. Roy, M. Parto, R. Nehra, C. Leefmans, and A. Marandi, Topological optical parametric oscillation, *Nanophotonics* **11**, 1611 (2022).
- [83] C. C. Wanjura, M. Brunelli, and A. Nunnenkamp, Topological framework for directional amplification in driven-dissipative cavity arrays, *Nat. Commun.* **11**, 3149 (2020).
- [84] T. Ramos, J. J. García-Ripoll, and D. Porras, Topological input-output theory for directional amplification, *Phys. Rev. A* **103**, 033513 (2021).
- [85] Á. Gómez-León, T. Ramos, A. González-Tudela, and D. Porras, Driven-dissipative topological phases in parametric resonator arrays, *Quantum* **7**, 1016 (2023).
- [86] Z. Gong, Y. Ashida, K. Kawabata, K. Takasan, S. Higashikawa, and M. Ueda, Topological Phases of Non-Hermitian Systems, *Phys. Rev. X* **8**, 031079 (2018).
- [87] N. Okuma and M. Sato, Non-Hermitian topological phenomena: A review, *Annu. Rev. Condens. Matter Phys.* **14**, 83 (2023).
- [88] L.-L. Wan and X.-Y. Lü, Quantum-Squeezing-Induced Point-Gap Topology and Skin Effect, *Phys. Rev. Lett.* **130**, 203605 (2023).